remote sensing

MDPI

Technical Note

Soil Moisture Retrieval from Multi-GNSS Reflectometry on FY-3E GNOS-II by Land Cover Classification

Cong Yin [1,2,3,4,†], Feixiong Huang [1,2,3,4,†], Junming Xia [1,2,3,4,*], Weihua Bai [1,2,3,4,5], Yueqiang Sun [1,2,3,4,5], Guanglin Yang [6], Xiaochun Zhai [6], Na Xu [6], Xiuqing Hu [6], Peng Zhang [6], Jinsong Wang [6], Qifei Du [1,2,3,4], Xianyi Wang [1,2,3,4] and Yuerong Cai [1,2,3,4]

1 National Space Science Center, Chinese Academy of Sciences, Beijing 100190, China
2 Beijing Key Laboratory of Space Environment Exploration, Chinese Academy of Sciences, Beijing 100190, China
3 Joint Laboratory on Occultations for Atmosphere and Climate, National Space Science Center, Chinese Academy of Sciences, Beijing 100190, China
4 Key Laboratory of Science and Technology on Space Environment Situational Awareness, Chinese Academy of Sciences, Beijing 100190, China
5 School of Astronomy and Space Science, University of Chinese Academy of Sciences, Beijing 100049, China
6 National Satellite Meteorological Center, China Meteorological Administration, Beijing 100081, China
* Correspondence: xiajunming@nssc.ac.cn
† These authors contributed equally to this work.

Abstract: The reflected GNSS signals at the L-band is significantly advantageous in soil moisture monitoring as they are sensitive to the dielectric properties determined by the volumetric water content of topsoil, and they can penetrate vegetation, except in very dense forests. The Global Navigation satellite system Occultation Sounder (GNOS-II) with a reflectometry technique onboard the Fengyun-3E (FY-3E) satellite, launched on 5 July 2021, is the first mission that can receive reflected Global Navigation Satellite System (GNSS) signals from GPS, BeiDou and Galileo systems. This paper presents the soil moisture retrieval results from the FY-3E GNOS-II mission using 16 months of data. In this study, the reflectivity observations from different GNSS systems were firstly intercalibrated with some differences analyzed. Observations were also corrected by considering vegetation attenuation for 16 different land cover classifications. Finally, an empirical model was constructed for volumetric soil moisture (VSM) estimation, where the reflectivity of GNOS-II was linearly related to the SMAP reference soil moisture for each 36 km ease grid. The overall root-mean-square error of the retrieved soil moisture is 0.049 compared with the SMAP product, and 0.054 compared with the in situ data. The results of the three GNSS systems show similar levels of accuracy. This paper, for the first time, demonstrates the feasibility of global soil moisture retrieval using multiple GNSS signals.

Keywords: GNOS-II; FY-3E; GNSS-R; volumetric soil moisture

Citation: Yin, C.; Huang, F.; Xia, J.; Bai, W.; Sun, Y.; Yang, G.; Zhai, X.; Xu, N.; Hu, X.; Zhang, P.; et al. Soil Moisture Retrieval from Multi-GNSS Reflectometry on FY-3E GNOS-II by Land Cover Classification. *Remote Sens.* **2023**, *15*, 1097. https://doi.org/10.3390/rs15041097

Academic Editors: Mehrez Zribi and Raffaele Albano

Received: 15 December 2022
Revised: 6 February 2023
Accepted: 12 February 2023
Published: 17 February 2023

1. Introduction

Soil moisture is a crucial factor that affects the transfer of water and heat energy between the surface of the soil and the boundary layer atmosphere through the processes of evaporation and transpiration by plants [1,2]. Assessing surface soil moisture is critical for refining short- and medium-term meteorological models, monitoring plant growth, and assisting in the early warning for natural calamities such as floods and droughts [3,4].

Remote sensing of soil moisture from space enables measurements with global coverage. Observations at low microwave frequencies are optimal for soil moisture monitoring because the signals are unaffected by weather conditions and less energy is attenuated by biomass. Both SMOS (soil moisture and ocean salinity) and SMAP (soil moisture active passive) are typical passive microwave spaceborne missions operating at the L-band (1.4 GHz), offering global soil moisture measurements at a resolution of 36~40 km, with a revisit period of about 3 days [5,6].

Global Navigation Satellite System Reflectometry (GNSS-R) is an emerging technique using navigation signals that are reflected off the earth surface for remote sensing applications. In 2003, the first remote sensing observations utilizing GNSS reflected signals from an orbit of 680 km were carried out by the United Kingdom Disaster Monitoring Constellation (UK-DMC) [7]. Subsequently, the United Kingdom TechDemoSat-1 (UK TDS-1) was launched in 2014 [8], with an orbit altitude of 635 km and an inclination of 98.4 degrees, providing worldwide GNSS-R measurements of the sea surface, land and cryosphere. To prioritize cyclone monitoring observations between $\pm 38^{\circ}$ latitude, NASA launched the Cyclone Global Navigation Satellite System (CYGNSS) in 2016. This constellation consisting of eight tiny satellites has an orbit altitude of 510 km and an inclination of 35 degrees [9].

Though numerous GNSS-R missions have been reported in the literature, there is little investigation on the spaceborne GNSS-R data from BeiDou (BDS) and Galileo (GAL) navigation satellite systems. The Fengyun-3E (FY-3E) satellite, carrying the Global Navigation Satellite System Occultation Sounder II (GNOS-II), was launched on 5 July 2021 [10]. The satellite orbits at an altitude of 836 km and has an inclination of 98.75 degrees, providing global coverage between ± 85 degrees for ionosphere, neutral atmosphere, and earth surface monitoring. As the upgraded version of the GNOS onboards the FY-3C and FY-3D, GNOS-II combines GNSS radio occultation and GNSS reflectometry. Meanwhile, the GNOS-II has eight reflection channels, allowing it to simultaneously track eight different navigation satellites. After one year of in-orbit testing with GPS and BDS signals, the Galileo signal acquisition was enabled on 7 July 2022 by switching one BDS channel to GAL channel. The GNOS-II payload will also be onboard FY-3F and FY-3G to construct a GNSS-R observation constellation, providing Earth observations with greater spatial coverage and temporal resolution [11]. The GNOS-II receiver is able to collect 300,000 reflections each day, of which approximately 27% are from land surfaces.

With a similar frequency to SMOS and SMAP, GNSS reflectometry shows great potential for land applications including monitoring of soil moisture [12–16], vegetation biomass [17,18], inland waterbodies [19,20] and freeze–thaw [21,22]. Meanwhile, GNSS-R has the potential for a better spatial resolution than the radiometer, and the observations are not affected by surface temperature. Using GNSS-R for land soil moisture retrieval was first demonstrated by several aircraft experiments [23,24]. There are also several approaches for GNSS-R soil moisture retrieval from space, including empirical change detection [13], multivariate regression [15] and neural network approach [16]. The empirical change detection is similar to the ASCAT soil moisture algorithm [25], and it was used for CYGNSS soil moisture product generation. This paper is also based on this method.

In this study, the reflectivity of BDS/GPS/GAL reflected signals derived from the Level 1 data of GNOS-II reflectometry are utilized for soil moisture estimation. The information about GNOS-II Level 1 data, SMAP reference data, and in situ observation data is provided in Section 2. The intercalibration and retrieval method are described in Section 3. Observations from different systems were calibrated to establish a general retrieval model. Since the GNSS-R observations are sensitive to roughness and topography, the model is developed for each ease grid of 36 km, and the vegetation effect is considered for different land classifications. Results and discussion are presented in Section 4. The retrieval accuracy was evaluated by comparing to both SMAP data and in situ measurements. Finally, conclusions are drawn in Section 5.

2. Materials

2.1. GNOS-II Data and Observable

The retrieval model for soil moisture was developed based on GNOS-II Level 1 data spanning approximately one year, from July 2021 to June 2022. Data from July 2022 to October 2022 were than used for validation. The mean revisit time (temporal resolution) at 36 km is around 12 days when the AM/PM overpasses are combined for the retrieved GNOS-R soil moisture. The GNSS signals received by the instrument are GPS L1 C/A, BDS

B1I and GAL E1B. Table 1 shows the differences between the three types of signals. Note that GAL signals are received in a subcarrier mode, resulting an equivalent chipping rate of 2.046 MHz [26]. The coherent integration time is 1 ms, and the incoherent integration time is 1 s.

Table 1. Characteristic of different GNSS signals received by GNOS-II.

	GPS L1 C/A	BDS B1I	GAL E1B
Frequency (MHz)	1575.42	1561.098	1575.42
Modulation	BPSK	BPSK	BOC(1,1)
Chipping rate (Mcps)	1.023	2.046	2.046
Code length (ms)	1	1	4

In GNOS-II Level 1 data, the reflected GNSS signal is processed into Delay-Doppler Map (DDM) in raw counts. Different from previous GNSS-R missions, GNOS-II uses 122×20 non-uniform Delay Doppler maps, where 1/8 chip delay interval is used for delay around the specular point between $[-3, 2.875]$ chips, and the 1/4 chip interval is used for the rest delay range. This enables high precision measurement around the specular point while achieving the delay range of $[-12.25, 12.125]$. Some examples of DDMs over land from BDS/GPS/GAL channels are shown in Figure 1. The samples are collected from a plain area, so the energy is concentrated at the peak. Different from the DDMs of GPS and BDS systems, the GAL DDM waveform has two side-lobes due to the BOC modulation. In addition to the observed DDM waveforms, metadata could also be extracted from the Level 1 data, including the DDM observation time in UTC, the position of receiver and transmitter satellites, the latitude and longitude of specular points, the PRN code of GNSS satellites, the gain of the reflected antenna, the incidence angle of observations, etc.

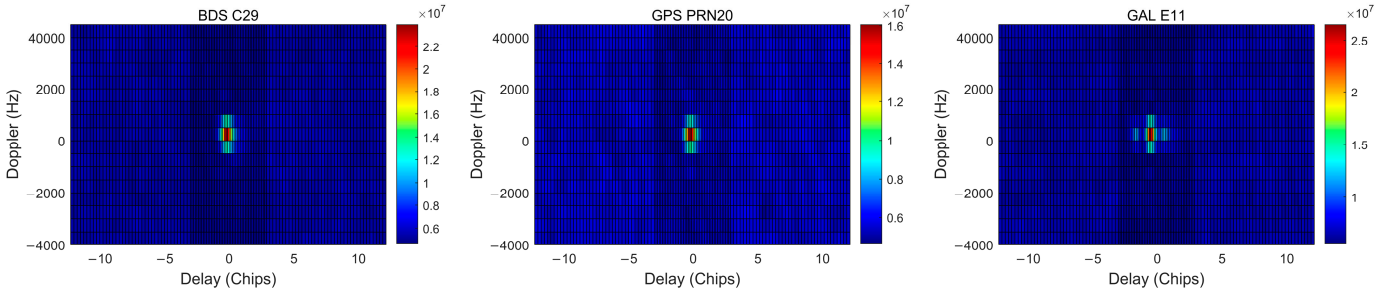

(**a**) (**b**) (**c**)

Figure 1. DDMs over the land surface from (**a**) BDS C29, (**b**) GPS PRN20 and (**c**) GAL E11.

Generally, it is assumed that the coherent reflections predominate in the GNSS-R signal over land, so the spatial resolution will be restricted to the first Fresnel zone [12]. At an altitude of around 830 km, the cross-track spatial resolution of the GNOS-II measurements of land surface is about 1 km. However, due to the 1 s incoherent integration time and the fact that the specular point travels around 5.8 km on the earth surface in one second, the resolution in the along-track direction is around 6 km.

A flag identifying the surface type in the Level 1 data was used to select DDMs acquired over land, along with various quality flags. Since GNOS-R prioritizes sea surface wind monitoring, the digital elevation map was not employed in the receiver during the in-orbit testing phase. Considering that observations of highlands are now unavailable, instead of using the delay offset flag in the Level 1 data to eliminate these observations, the delay offset and the difference between the estimated peak delay and observed DDM peak delay were calculated using Equations (1) and (2).

$$delay\_offset = -2 \cdot h \cdot \cos(\theta_{inc})/chip\_length \quad (1)$$

where h represents the height from the Digital Elevation Model (DEM) at a resolution of 10 km, θ_{inc} represents the incidence angle; the *chip_length* is 150 m for BDS and GAL, and 300 m for GPS.

The difference between the calculated *delay_offset* and *ddm_peak_delay* is

$$delay\_diff = delay\_offset - ddm\_peak\_delay \quad (2)$$

Only DDMs with an absolute value of *delay_offset* less than 12 chips and an absolute value of *delay_diff* less than 3 chips are exploited to ensure that the observations are valid.

2.2. SMAP Reference Data

The enhanced SMAP L3 radiometer volumetric soil moisture at a resolution of 9 km was used for reference data, and the vegetation water content derived from SMAP was used for vegetation optical thickness calculation in the $\tau - \omega$ model. The SMAP also operates in the sun-synchronous orbit and measures the bright temperature for soil moisture estimation at the local time of 6:00 (descending) and 18:00 (ascending), which is similar to FY-3E. However, the observed trajectories of GNOS-R and SMAP do not coincide well. As shown in Figure 2a, the green tracks indicate the overlap of two measurements, while the red tracks represent the GNOS-R observations not coincident with the SMAP measurements. Thus, three days of SMAP product were averaged for comparison, including ascending and descending passes. As shown in Figure 2b, almost every track match succeeds except for observations over inland waterbody and snow/ice that are not applicable for soil moisture retrieval.

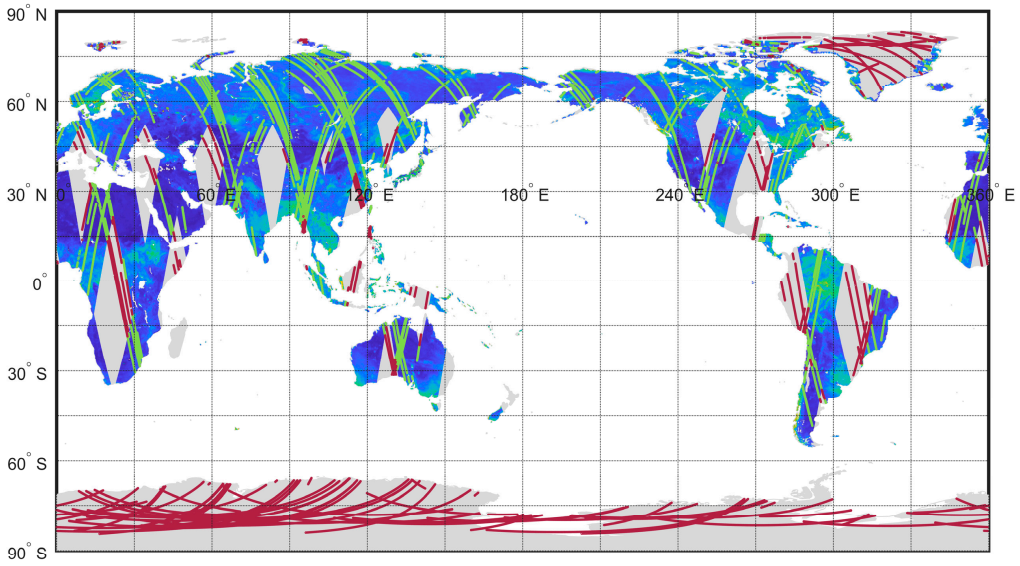

(**a**)

Figure 1. *Cont.*

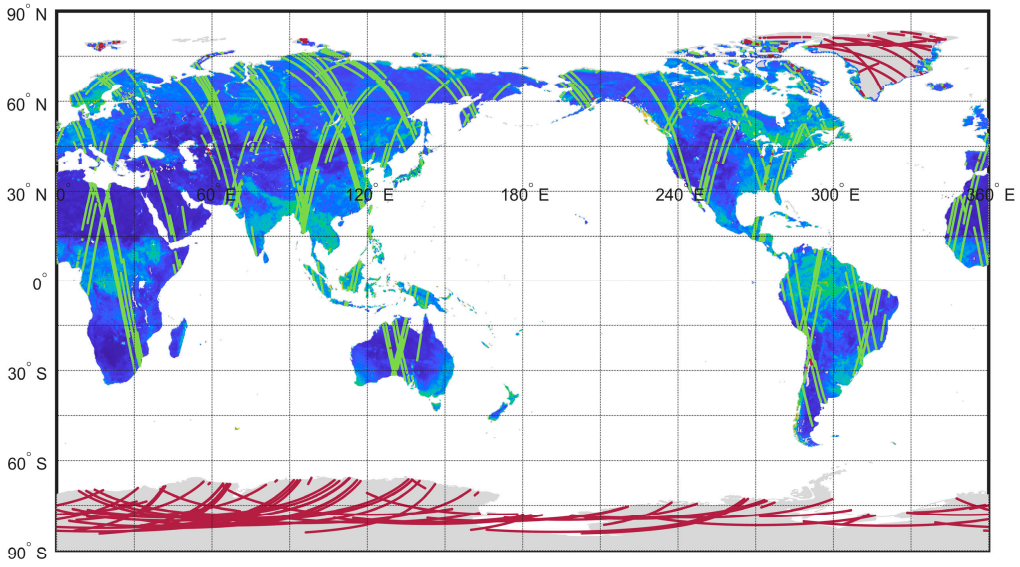

(**b**)

Figure 2. The overlap between GNOS-II tracks and SMAP tracks (**a**) The overlap between GNOS-II tracks and SMAP observations in one day (**b**) The overlap between GNOS-II tracks and SMAP observations in three days (the green tracks indicate the overlap of two measurements, whereas the red tracks represent the GNOS-R observations that are not coincident with the SMAP measurements).

2.3. ISMN In-Situ Soil Moisture Network

The International Soil Moisture Network (ISMN) observations of in situ soil moisture were used for validation. The ISMN provides a database of in situ soil moisture measurements from 74 soil moisture networks worldwide [27]. By selecting observations from 10 July 2021 to 31 October 2022, the data of 260 stations were taken for comparison in this study, as shown in Figure 3. Most of the stations are located in the United States.

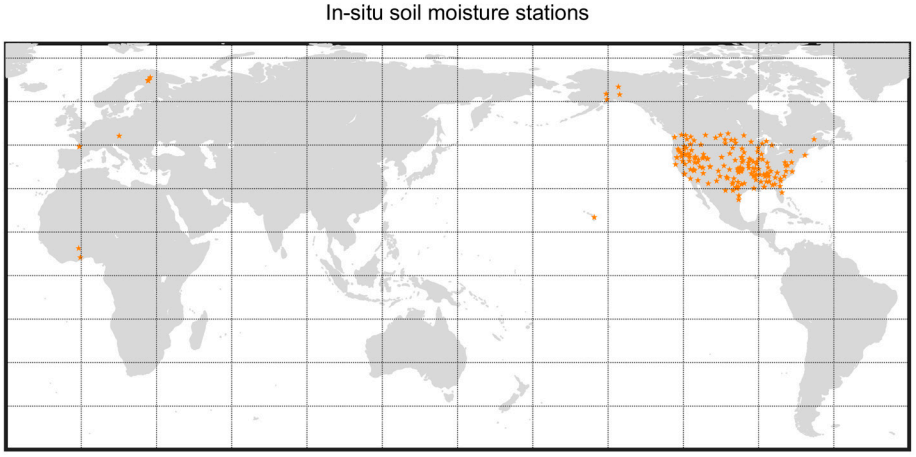

Figure 3. Distribution of in situ soil moisture stations.

3. Methods

3.1. Calibration of Reflectivity from Multi-GNSS Observations

The DDMs in raw counts collected by the receiver are firstly calibrated to the DDM power using the instrument gain, G,

$$P = C/G \tag{3}$$

where C is the DDM in raw counts and P is the DDM power. The instrument gain is different for each GNSS system, measured by a pre-launch experiment [11]. The reflectivity under coherent reflection can be calculated as follows [15]:

$$\Gamma(\theta) = \frac{(4\pi)^2 (P_r - N)(R_r + R_t)^2}{\lambda^2 P_t G_t G_r} \quad (4)$$

where θ is the incidence angel; P_r is the peak power of the DDM; N is the noise floor; R_t and R_r are the distance from the transmitter and the receiver to the specular point, respectively, $P_t G_t$ is the transmitter equivalent isotropic radiated power (EIRP) measured by a static station in Beijing, China; G_r is the reflected antenna gain; λ is the wavelength of GNSS signals, i.e., 0.1921 m for BDS and 0.1903 m for GPS and GAL.

It is important to intercalibrate the reflectivity observations from the three systems before applying any retrieval method so that the observations are consistent and can be retrieved by a same model. Because of the complications that observations over land can be coherent and incoherent depending on the surface roughness, we first analyzed the reflectivity over sea ice since most observations over sea ice can be perfectly coherent. Four months of data from July 2022 to October 2022 (since the Galileo channel was enabled) were used for the analysis. Observations over sea ice with sea ice concentration (SIC) larger than 15% from either two systems were collocated when they locate in the same ease grid of 9 km on the same day. The SIC data are from the OSISAF sea ice concentration product [28]. According to our analysis, most signals are coherent when the SIC is larger than 15%. Figure 4 shows the comparison of reflectivity over sea ice from different systems. It is observed that the reflectivity from the three systems agree well with each other. This indicates that the calibration of the instrument gain in Equation (3), along with the transmitter EIRP and reflected antenna gain in Equation (4), has negligible bias.

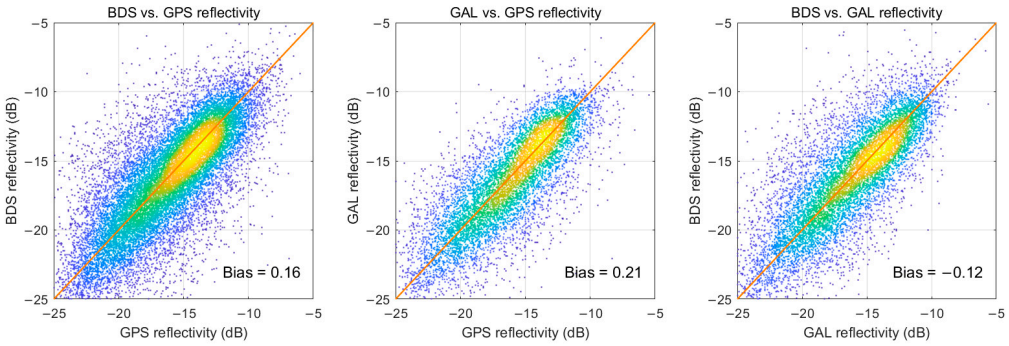

Figure 4. Density scatter plots for the comparison between reflectivity over sea ice from different GNSS systems (7 July–31 October 2022). Bias is also displayed on each sub-figure.

Then, in the same way, we collocated the observations over land from different systems when they locate in the same 9 km ease grid on the same day. The comparison of reflectivity over land from different systems is shown in Figure 5a. It is found that the reflectivity of BDS and GAL are close, whereas the reflectivity of GPS is a little higher than the others. This is because some observations over land are incoherent scattering and the reflected power under incoherent scattering is related to the scattering area [29]. As shown in Table 1, because GPS signals have a lower chipping rate, its chip length (~300 m) is twice of that of BDS and GAL (~150 m), resulting a larger scattering area. There is also a minor difference in the scattering area of BDS and GAL due to the difference in the signal modulation. A detailed comparison of scattering area of the three systems under incoherent scattering can be found in [30].

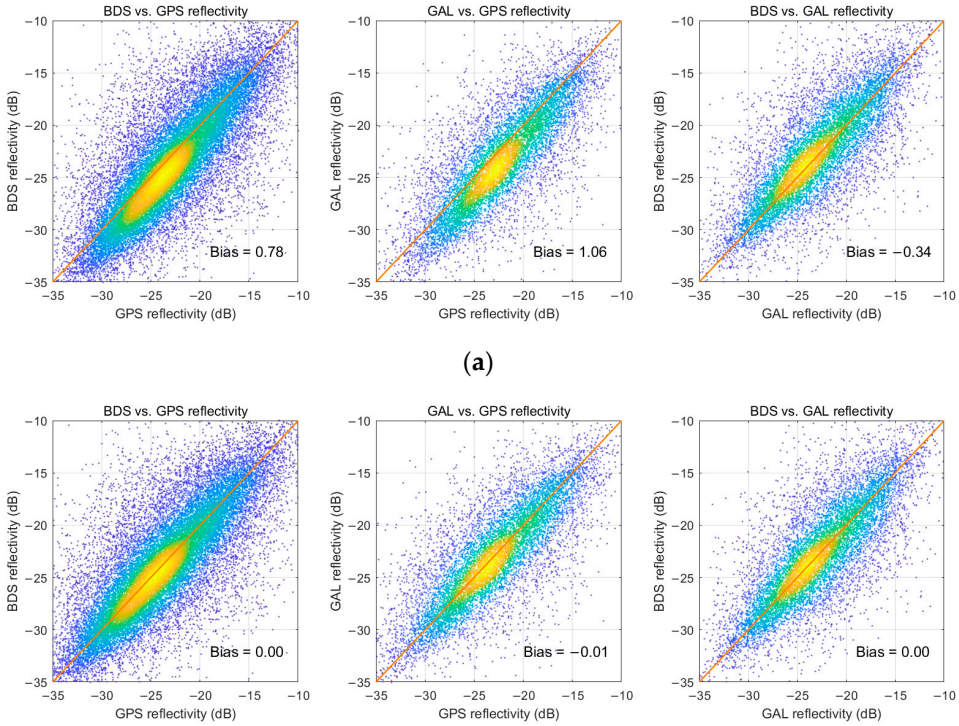

Figure 5. Density scatter plots for the comparison between reflectivity from different GNSS systems (7 July–31 October 2022): (**a**) before calibration; (**b**) after calibration.

In this work, GPS reflectivity and Galileo reflectivity are calibrated to be consistent with BDS reflectivity by using linear calibration coefficients in Table 2. P1 represents the slope, and P2 represents the intercede. The comparison of calibrated reflectivity of the three systems is displayed in Figure 5b; they are shown to be in agreement with each other. In this way, a general retrieval model can be applied to observations from the three systems. The GNOS-II reflectivity of the global land surface is shown in Figure 6.

Table 2. Calibration coefficient for different systems.

Calibration Coefficients	P1	P2
GPS	1.075	0.94
BDS	1	0
GAL	1	0.34

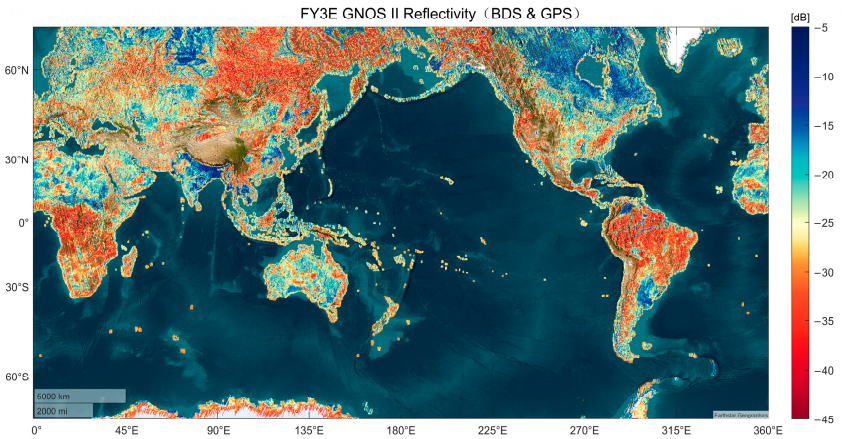

Figure 6. The GNOS-II reflectivity of land surface (10 July–9 September 2021).

The reflectivity is related to several physical characteristics of land surface. Firstly, due to the surface soil dielectric constant, soil moisture has a primary influence on reflectivity over land surface with low vegetation (<5 kg/m^2) and flat terrain. Secondly, vegetation attenuation plays an important role in high vegetation areas, e.g., over tropical forests. Thirdly, surface roughness also has an effect on the reflectivity due to yielding diffuse scattering. It is worth noting that for spaceborne observations, the impacts of topography are more substantial than those of small-scale roughness [29].

3.2. Correction for Vegetation Attenuation

As the GNSS reflected signals are absorbed by the vegetation canopy, the observed reflectivity can be corrected to the reflectivity of the soil surface [31]:

$$\Gamma_{soil}(\theta) = \Gamma(\theta)/\gamma \tag{5}$$

where Γ is the observed reflectivity calculated by Equation (4); Γ_{soil} is the reflectivity of soil surface; θ is the incidence angle; γ is the two-way attenuation of biomass canopy derived as

$$\gamma = \exp(-2 \cdot b \cdot vwc/\cos(\theta)) \tag{6}$$

where *vwc* is the vegetation water content derived from the SMAP soil moisture product at a resolution of 9 km; b is a constant parameter depends on signal wavelength, polarization, and vegetation classification. For a wavelength of about 20 cm, the parameter b ranges from 0.09 to 0.15 under different land cover classifications [32]. In this study, an IGBP look-up table was employed for IGBP classification, and the value of b was set according to the SMAP ATBT document for each IGBP class, as indicated in Table 3 [33].

Table 3. The setting of parameter b according to IGBP classifications.

IGBP	b
Evergreen Needleleaf Forest	0.10
Evergreen Broadleaf Forest	0.10
Deciduous Needleleaf Forest	0.12
Deciduous Broadleaf Forest	0.12
Mixed Forest	0.11
Closed Shrublands	0.11
Open Shrublands	0.11
Woody Savannas	0.11
Savannas	0.11
Grasslands	0.13
Permanent Wetlands	0
Croplands	0.11
Urban and Built-Up	0.10
Cropland Natural Vegetation Mosaic	0.11
Snow and Ice	0.11
Barren or Sparsely Vegetated	0.11

3.3. Analysis of Terrain Roughness Attenuation

For spaceborne GNSS-R measurements, large-scale roughness has a greater impact on DDM observations. This subsection presents an analysis of the terrain roughness attenuation on the observations of GNOS-II. Although there are two effects linked to topography and micro-topography, it is difficult to separate them. Thus, we compute the combined effect of both. The roughness attenuation effects could be represented below:

$$Att_{\text{roughness}} = \Gamma_{soil}/\Gamma_{fresnel} \tag{7}$$

The reflectivity of the soil surface Γ_{soil} could be calculated with Equations (4) and (5), and the Fresnel reflectivity $\Gamma_{fresnel}$ dependent on the surface soil dielectric constant ε and the incidence angle θ [31]:

$$\Gamma_{fresnel} = |R_{rl}(\theta)|^2 = \frac{(\varepsilon - 1)^2 \cos^2\theta(\varepsilon - \sin^2\theta)}{\left(\varepsilon\cos\theta + \sqrt{\varepsilon - \sin^2\theta}\right)^2 \left(\cos\theta + \sqrt{\varepsilon - \sin^2\theta}\right)^2} \quad (8)$$

where R_{rl} represents the Fresnel reflection coefficient, and θ is the incidence of the observation. Note that for GNSS-R measurements, the transmitted signal is in right hand circular polarization, and the reflected signal is in left hand circular polarization. The soil dielectric constant ε could be obtained using the Mironov dielectric constant model, with clay fraction, soil moisture reference data, and signal frequency as the inputs [34]:

$$\varepsilon = \text{mironov}(\text{C}, \text{mv}, \text{freq}) \quad (9)$$

where C is the clay fraction obtained from the Open Land Map [35] and grided to ease grid of 9 km, mv is the soil moisture in volumetric from the SMAP soil moisture product at a resolution of 9 km, freq is the frequency of reflected signals from different GNSS systems.

The soil dielectric constant was calculated from Equation (9). Then, the Fresnel reflectivity could be obtained by Equation (8). Finally, the predicted global roughness (topography) attenuation at a resolution of 36 km is presented in Figure 7. The predicted values on different incidence angles were averaged on each grid. Regions with high elevations have larger attenuation (negative value) because complicated terrain is usually found at high altitudes. Due to the spatial heterogeneity of topography, it is difficult to construct a model for worldwide application. For this reason, instead of constructing a physical model, the empirical change detection approach [13] is used in this study.

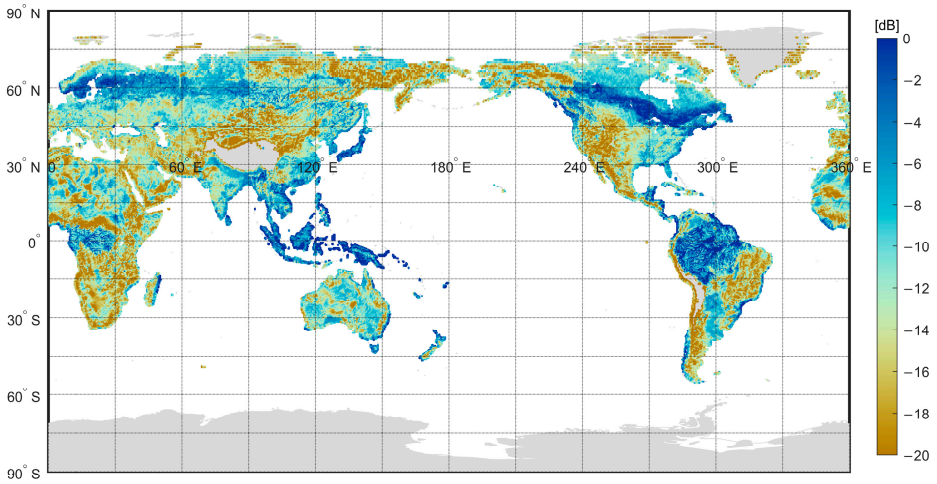

Figure 7. The estimated topography attenuation at an ease grid of 36 km.

3.4. Soil Moisture Retrieval

The algorithm in this study assumes that, given a certain location, the only variables that change over time are soil moisture and biomass, whereas the soil surface roughness (topography) and soil texture remain constant. In this case, the reflectivity of GNOS-II could be linearly related to the SMAP reference soil moisture at each ease grid cell [13].

$$sm = a \cdot \Gamma_{soil} + b \quad (10)$$

where sm represents the reference data of soil moisture; parameters a and b are polynomial fitting coefficients, Γ_{soil} is the observed reflectivity with vegetation correction, which could be derived from Equations (4)–(6).

The coefficients a and b were fitted for every ease grid of 36 km, and the SMAP soil moisture at a resolution of 9 km was used as the reference value for sm. One-year observations (July 2021–June 2022) were used for the model development. There are about 100 specular points in average in each 36 km grid in the training. No separation by GNSS systems was made in this training step. The incidence angle will also affect the coherent reflectivity. This effect only becomes substantial when the incidence angle exceeds 50 degrees. GNOS-II has a maximum incidence angle of 53 degrees, with most observations concentrated in the range of (15, 45) degrees as shown in Figure 8. Thus, the incidence influence was ignored in this study.

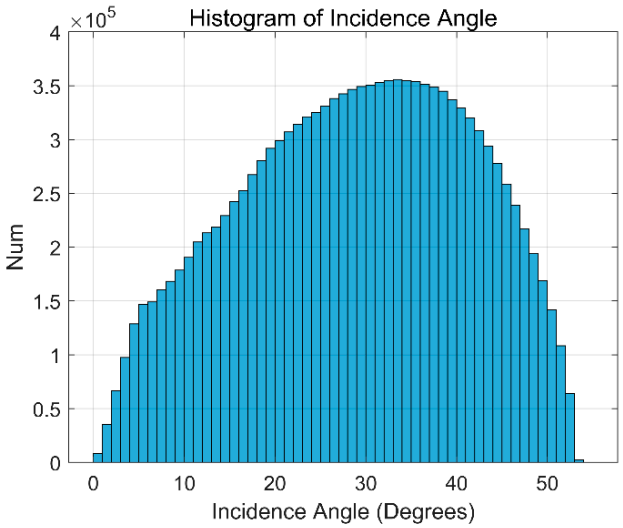

Figure 8. The histogram of the incidence angles for the observations of FY-3E GNOS-II.

4. Results and Discussion

During the model development, one-year observations (since 10 July 2021 to 28 June 2022) were utilized. The model was then applied to GNOS-II data to retrieve soil moisture from July to October 2022. As an illustration, the retrieved FY-3E GNOS-II soil moisture results of one month, from 7 July to 6 August 2022, are shown in Figure 9.

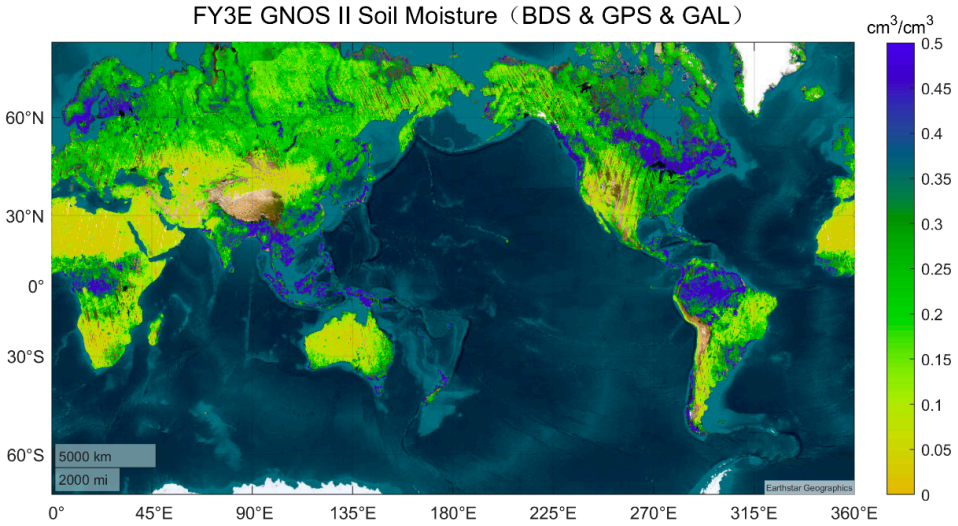

Figure 9. GNOS-II global soil moisture estimation (7 July–6 August 2022).

4.1. Comparison with SMAP

The GNOS-II soil moisture estimations were compared with SMAP reference data on a global scale with the independent test set. The test set is from 7 July 2022 to 5 August 2022, and from 5 October 2022 to 31 October 2022. A gap was found in the comparison because the SMAP data acquisition was interrupted for almost two months. The density scatter plots of GNOS-II soil moisture results from GPS/BDS/GAL reflections versus SMAP soil moisture reference data are shown in Figure 10. For data with a vegetation water content below 5 kg/m^2, the overall RMSE of the estimated soil moisture was 0.0503 cm^3/cm^3 for GPS, 0.0497 cm^3/cm^3 for BDS, and 0.0482 cm^3/cm^3 for GAL at volumetric water content, with a correlation coefficient of 0.83, 0.85 and 0.86, respectively, as shown in Table 4. The three systems have similar measurement accuracy. The overall RMSE is 0.0490 cm^3/cm^3. The results indicate that soil moisture retrieval with reflected signals from different GNSS systems is feasible, which enables GNSS-R observations to have improved spatial and frequency coverage.

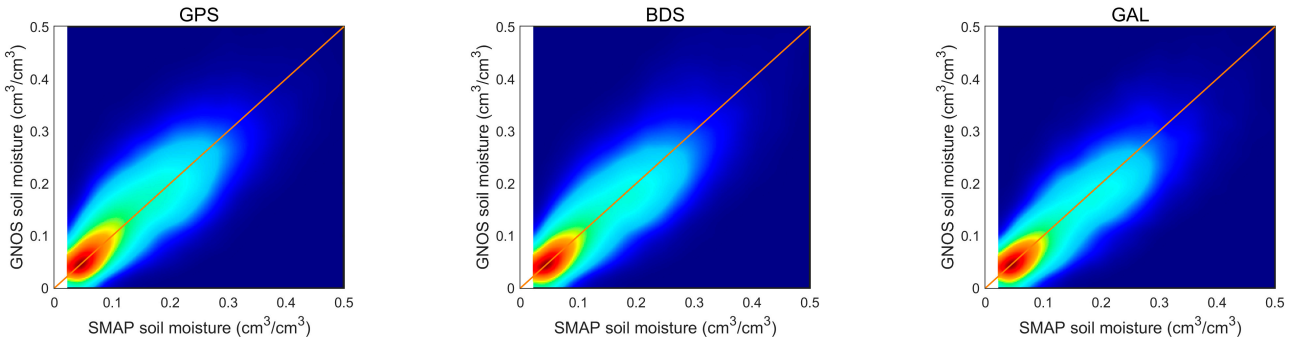

Figure 10. GNOS-II soil moisture vs. SMAP soil moisture. (**a**) GPS; (**b**) BDS; (**c**) GAL.

Table 4. The RMSE and correlation coefficient between GNOS-II and SMAP soil moisture.

SYSTEM	GPS	BDS	GAL
RMSE (cm^3/cm^3)	0.0500	0.0499	0.0482
Correlation Coefficient	0.83	0.85	0.86

4.2. Comparison with ISMN

Additionally, observations from in situ stations were also utilized for product validation. Overall, 16 months of FY-3E GNOS-II data from July 2021 to October 2022 were used in this comparison. Comparison data were obtained from the ISMN networks. For each site, GNOS-II specular points located in the same ease grid of 36 km were selected, and the time-matching window is one day. For each observation technique, observations from a single day were averaged. As suggested in Section 4.1, data from the three GNSS systems have similar accuracy. Therefore, The GNOS-R soil moisture retrieved from GPS/BDS/GAL are combined for validation, to obtain more matching data. Some examples of comparing GNOS-II soil moisture time series with in situ measurements are illustrated in Figure 11. The histograms of the ubRMSE between GNOS/SMAP soil moisture and ISMN in situ observations are represented in Figure 12. The average ubRMSE of GNOS-II soil moisture estimations is 0.054 cm^3/cm^3.

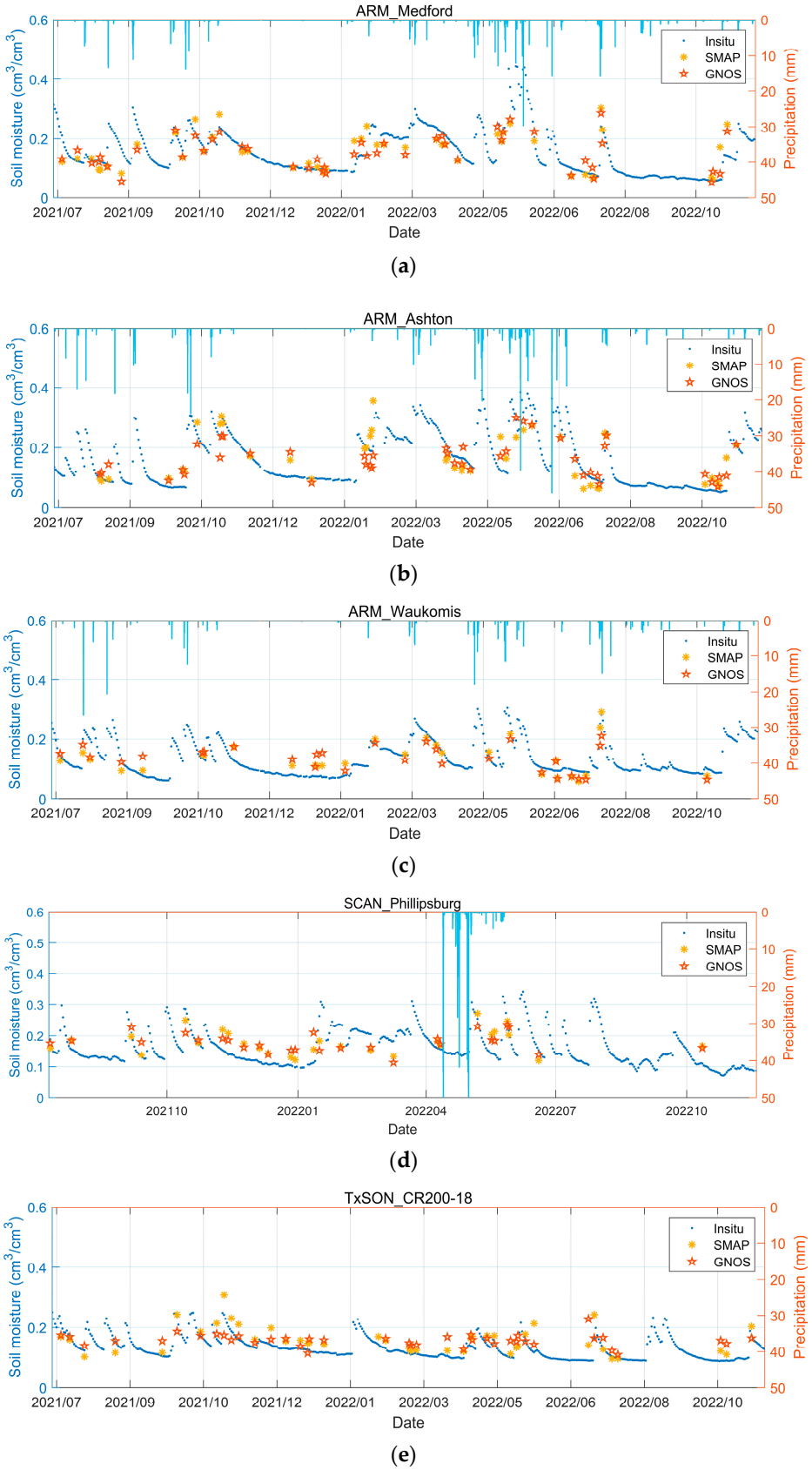

Figure 11. GNOS/SMAP soil moisture vs. ISMN in situ observations. (**a**) ARM Medford; (**b**) ARM Ashton; (**c**) ARM Waukomis; (**d**) SCAN Phillipsburg; (**e**) TxSON CR 200-18.

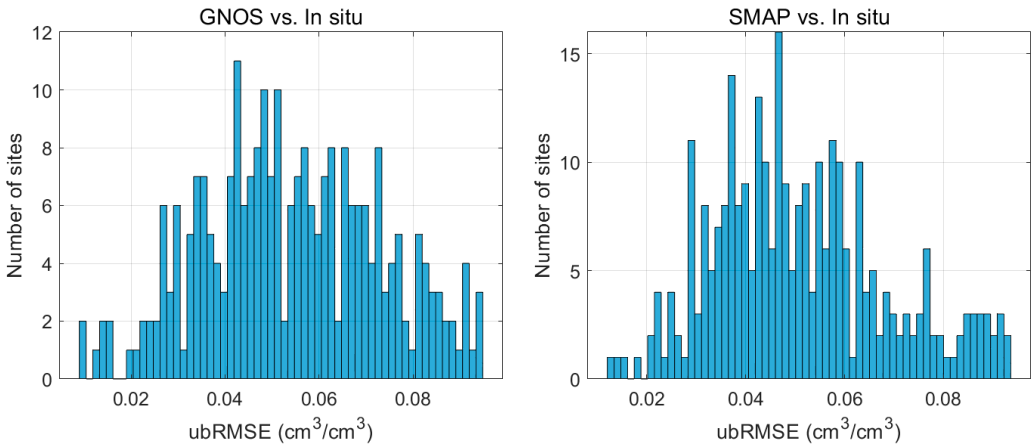

(**a**) (**b**)

Figure 12. The histogram of ubRMSE (**a**) GNOS vs. in situ (**b**) SMAP vs. in situ.

4.3. Discussion

Generally, there are two types of retrieval methods for multi-GNSS reflectometry observations: First, use different retrieval models for different systems; Second, calibrate observables from different systems to a same level and use a general retrieval model for them. The first type is simple but not good for data fusion and cross-satellite validation. This study utilized the second type of method which requires careful intercalibration among GNSS systems. The observations under full coherent reflection from different systems should be consistent as the received power only depends on the size of first Fresnel Zone which should be almost same as the GNSS signals (at least for GPS L1, BDS B1 and GAL E1) have similar carrier frequency. However, observations under incoherent scattering depend on the scattering area which is related to the chip length and signal modulation, resulting a discrepancy of observations between GNSS systems. This paper empirically calibrated reflectivity observations of the three systems to a same level in order to apply a common retrieval model. This method can be further improved if coherent and incoherent components can be accurately distinguished.

So far, the empirical model in this study was constructed on 36 km ease grid. However, due to the high heterogeneity of land surface, model with higher spatial resolution is essential. The ongoing study will attempt to establish the model on 9 km or 6.25 km ease grid with more observational data. Due to the incoherent integration time of 1 s, the along-track resolution for FY-3E GNOS-II observations is restricted to 6 km. In order to increase spatial resolution for terrestrial applications, it is planned to reduce the incoherent integration time in subsequent GNSS-R missions.

The soil moisture retrieval model requires auxiliary data sets to compute the attenuation effects of vegetation and roughness (topography). The optical thickness of vegetation could be estimated with SMAP vwc ancillary data. However, it is difficult to find appropriate ancillary data for roughness (topography) attenuation estimation because only a small-scale RMS height was considered in most soil roughness ancillary data, whereas large-scale roughness (topography) has a larger influence on spaceborne GNSS observations. The extrapolated topography attenuation has obvious regional characteristics and could be related to the distribution of global topography. By assuming that the roughness/topography are constant for a certain region, and only soil moisture and vegetation vary with time, GNOS-II soil reflectivity was linearly fitted to the SMAP reference soil moisture for each ease grid of 36 km.

5. Conclusions

The FY-3E GNOS-II is the first multi-GNSS reflectometry mission that can monitor global soil moisture variation with GPS, BeiDou and Galileo signals. Reflectivity observations from the three systems were carefully intercalibrated under coherent and incoherent scattering. The effect of vegetation attenuation was also corrected by 16 land cover classifications. An empirical model was constructed on each 36 km ease grid by matching GNOS-II-observed reflectivity to SMAP soil moisture using one-year data from July 2021 to June 2022. Retrieved soil moisture from GNOS-II was validated by SMAP soil moisture and independent in situ measurements. Results from the three systems have the similar good retrieval accuracy. This paper, for the first time, demonstrates the global soil moisture using multiple GNSS signals, enabling a better spatiotemporal coverage.

Author Contributions: Conceptualization, Y.S., W.B., Q.D., X.W. and Y.C.; methodology, C.Y., F.H., J.X. and X.Z.; software, C.Y., J.X. and F.H.; validation, C.Y., J.X. and F.H.; resources, G.Y., X.Z., J.W., P.Z., Y.S., X.H. and N.X.; data curation, C.Y., J.X. and F.H.; writing—original draft preparation, C.Y.; writing—review and editing, F.H. and J.X.; project administration, G.Y., X.Z., J.W., P.Z., Y.S., X.H. and N.X.; funding acquisition, J.W., P.Z. and X.H. All authors have read and agreed to the published version of the manuscript.

Funding: This work is supported by the Key Program of Joint Fund of the National Natural Science Foundation of China and Shandong Province under Grant U22A20586, the National Natural Science Foundation of China under grant 42074042 and 42104032 and in part by the Youth Cross Team Scientific Research Project of the Chinese Academy of Sciences (JCTD-2021-10) and in part by the Feng Yun 3 (FY-3) Global Navigation Satellite System Occultation Sounder (GNOS and GNOS II) Development and Manufacture Project led by the National Space Science Center, Chinese Academy of Sciences (NSSC/CAS).

Data Availability Statement: The SMAP Enhanced 9 km Soil Moisture product is available at: https://nsidc.org/data/smap/data (accessed on 3 November 2022). The International Soil Moisture Network in situ soil moisture product is available at: https://ismn.earth/en/data/(accessed on 23 November 2022). The OSI SAF Sea Ice Concentration product is available at: https://osi-saf.eumetsat.int/products/osi-401-b (accessed on 11 November 2022).

Acknowledgments: The authors would like to acknowledge NASA NSIDC, ISMN, and OSI SAF, for providing the SMAP Enhanced L3 Radiometer Global and Polar Grid Daily 9 km EASE-Grid Soil Moisture data, the in situ soil moisture data and sea ice concentration data.

Conflicts of Interest: The authors declare no conflict of interest.

References

1. Drinkwater, M.; Kerr, Y.; Font, J.; Berger, M. Exploring the water cycle of the blue planet. The Soil Moisture and Ocean Salinity mission. *ESA Bull.* **2009**, *137*, 7–15.
2. Saux-Picart, S.; Ottlé, C.; Decharme, B.; André, C.; Zribi, M.; Perrier, A.; Coudert, B.; Boulain, N.; Cappelaere, B.; Descroix, L. Water and energy budgets simulation over the AMMA-Niger super-site spatially constrained with remote sensing data. *J. Hydrol.* **2009**, *375*, 287–295. [CrossRef]
3. Brocca, L.; Crow, W.T.; Ciabatta, L.; Massari, C.; De Rosnay, P.; Enenkel, M.; Hahn, S.; Amarnath, G.; Camici, S.; Tarpanelli, A. A review of the applications of ASCAT soil moisture products. *IEEE J. Sel. Top. Appl. Earth Obs. Remote Sens.* **2017**, *10*, 2285–2306. [CrossRef]
4. Koster, R.D.; Dirmeyer, P.A.; Guo, Z.; Bonan, G.; Chan, E.; Cox, P.; Gordon, C.; Kanae, S.; Kowalczyk, E.; Lawrence, D. Regions of strong coupling between soil moisture and precipitation. *Science* **2004**, *305*, 1138–1140. [CrossRef]
5. Kerr, Y.H.; Waldteufel, P.; Wigneron, J.-P.; Martinuzzi, J.; Font, J.; Berger, M. Soil moisture retrieval from space: The Soil Moisture and Ocean Salinity (SMOS) mission. *IEEE Trans. Geosci. Remote Sens.* **2001**, *39*, 1729–1735. [CrossRef]
6. Entekhabi, D.; Njoku, E.G.; O'Neill, P.E.; Kellogg, K.H.; Crow, W.T.; Edelstein, W.N.; Entin, J.K.; Goodman, S.D.; Jackson, T.J.; Johnson, J. The soil moisture active passive (SMAP) mission. *Proc. IEEE* **2010**, *98*, 704–716. [CrossRef]
7. Gleason, S.; Hodgart, S.; Sun, Y.; Gommenginger, C.; Mackin, S.; Adjrad, M.; Unwin, M. Detection and processing of bistatically reflected GPS signals from low earth orbit for the purpose of ocean remote sensing. *IEEE Trans. Geosci. Remote Sens.* **2005**, *43*, 1229–1241. [CrossRef]

8. Foti, G.; Gommenginger, C.; Jales, P.; Unwin, M.; Shaw, A.; Robertson, C.; Rosello, J. Spaceborne GNSS reflectometry for ocean winds: First results from the UK TechDemoSat-1 mission. *Geophys. Res. Lett.* **2015**, *42*, 5435–5441. [CrossRef]
9. Ruf, C.S.; Chew, C.; Lang, T.; Morris, M.G.; Nave, K.; Ridley, A.; Balasubramaniam, R. A new paradigm in earth environmental monitoring with the cygnss small satellite constellation. *Sci. Rep.* **2018**, *8*, 1–13. [CrossRef]
10. Zhang, P.; Hu, X.; Lu, Q.; Zhu, A.; Lin, M.; Sun, L.; Chen, L.; Xu, N. FY-3E: The first operational meteorological satellite mission in an early morning orbit. *Adv. Atmos. Sci.* **2022**, *39*, 1–8. [CrossRef]
11. Yang, G.; Bai, W.; Wang, J.; Hu, X.; Zhang, P.; Sun, Y.; Xu, N.; Zhai, X.; Xiao, X.; Xia, J. FY3E GNOS II GNSS Reflectometry: Mission Review and First Results. *Remote Sens.* **2022**, *14*, 988. [CrossRef]
12. Camps, A.; Park, H.; Pablos, M.; Foti, G.; Gommenginger, C.P.; Liu, P.-W.; Judge, J. Sensitivity of GNSS-R spaceborne observations to soil moisture and vegetation. *IEEE J. Sel. Top. Appl. Earth Obs. Remote Sens.* **2016**, *9*, 4730–4742. [CrossRef]
13. Chew, C.; Small, E. Description of the UCAR/CU soil moisture product. *Remote Sens.* **2020**, *12*, 1558. [CrossRef]
14. Al-Khaldi, M.M.; Johnson, J.T.; O'Brien, A.J.; Balenzano, A.; Mattia, F. Time-series retrieval of soil moisture using CYGNSS. *IEEE Trans. Geosci. Remote Sens.* **2019**, *57*, 4322–4331. [CrossRef]
15. Clarizia, M.P.; Pierdicca, N.; Costantini, F.; Floury, N. Analysis of CYGNSS data for soil moisture retrieval. *IEEE J. Sel. Top. Appl. Earth Obs. Remote Sens.* **2019**, *12*, 2227–2235. [CrossRef]
16. Eroglu, O.; Kurum, M.; Boyd, D.; Gurbuz, A.C. High spatio-temporal resolution CYGNSS soil moisture estimates using artificial neural networks. *Remote Sens.* **2019**, *11*, 2272. [CrossRef]
17. Santi, E.; Paloscia, S.; Pettinato, S.; Fontanelli, G.; Clarizia, M.P.; Comite, D.; Dente, L.; Guerriero, L.; Pierdicca, N.; Floury, N. Remote sensing of forest biomass using GNSS reflectometry. *IEEE J. Sel. Top. Appl. Earth Obs. Remote Sens.* **2020**, *13*, 2351–2368. [CrossRef]
18. Carreno-Luengo, H.; Luzi, G.; Crosetto, M. Above-ground biomass retrieval over tropical forests: A novel GNSS-R approach with CyGNSS. *Remote Sens.* **2020**, *12*, 1368. [CrossRef]
19. Loria, E.; O'Brien, A.; Zavorotny, V.; Downs, B.; Zuffada, C. Analysis of scattering characteristics from inland bodies of water observed by CYGNSS. *Remote Sens. Environ.* **2020**, *245*, 111825. [CrossRef]
20. Nghiem, S.V.; Zuffada, C.; Shah, R.; Chew, C.; Lowe, S.T.; Mannucci, A.J.; Cardellach, E.; Brakenridge, G.R.; Geller, G.; Rosenqvist, A. Wetland monitoring with global navigation satellite system reflectometry. *Earth Space Sci.* **2017**, *4*, 16–39. [CrossRef] [PubMed]
21. Comite, D.; Cenci, L.; Colliander, A.; Pierdicca, N. Monitoring freeze-thaw state by means of GNSS reflectometry: An analysis of TechDemoSat-1 data. *IEEE J. Sel. Top. Appl. Earth Obs. Remote Sens.* **2020**, *13*, 2996–3005. [CrossRef]
22. Rautiainen, K.; Comite, D.; Cohen, J.; Cardellach, E.; Unwin, M.; Pierdicca, N. Freeze–Thaw Detection Over High-Latitude Regions by Means of GNSS-R Data. *IEEE Trans. Geosci. Remote Sens.* **2021**, *60*, 1–13. [CrossRef]
23. Masters, D.; Axelrad, P.; Katzberg, S. Initial results of land-reflected GPS bistatic radar measurements in SMEX02. *Remote Sens. Environ.* **2004**, *92*, 507–520. [CrossRef]
24. Egido, A.; Paloscia, S.; Motte, E.; Guerriero, L.; Pierdicca, N.; Caparrini, M.; Santi, E.; Fontanelli, G.; Floury, N. Airborne GNSS-R Polarimetric Measurements for Soil Moisture and Above-Ground Biomass Estimation. *IEEE J. Sel. Top. Appl. Earth Obs. Remote Sens.* **2014**, *7*, 1522–1532. [CrossRef]
25. Bartalis, Z.; Naeimi, V.; Hasenauer, S.; Wagner, W. *ASCAT Soil Moisture Product Handbook*; ASCAT Soil Moisture Report Series, No. 15; Institute of Photogrammetry and Remote Sensing, Vienna University of Technology: Vienna, Austrilia, 2008.
26. Qiu, T.; Wang, X.; Sun, Y.; Li, F.; Wang, Z.; Xia, J.; Du, Q.; Bai, W.; Cai, Y.; Wang, D. An Innovative Signal Processing Scheme for Spaceborne Integrated GNSS Remote Sensors. *Remote Sens.* **2023**, *15*, 745. [CrossRef]
27. Dorigo, W.; Himmelbauer, I.; Aberer, D.; Schremmer, L.; Petrakovic, I.; Zappa, L.; Preimesberger, W.; Xaver, A.; Annor, F.; Ardö, J. The International Soil Moisture Network: Serving Earth system science for over a decade. *Hydrol. Earth Syst. Sci.* **2021**, *25*, 5749–5804. [CrossRef]
28. Tonboe, R.; Lavelle, J.; Pfeiffer, R.-H.; Howe, E. *Product user manual for osi saf global sea ice concentration*; Product OSI-401-b; Danish Meteorological Institute: Copenhagen, Denmark, 2017.
29. Yueh, S.H.; Shah, R.; Chaubell, M.J.; Hayashi, A.; Xu, X.; Colliander, A. A semiempirical modeling of soil moisture, vegetation, and surface roughness impact on CYGNSS reflectometry data. *IEEE Trans. Geosci. Remote Sens.* **2020**, *60*, 1–17. [CrossRef]
30. Huang, F.; Xia, J.; Yin, C.; Zhai, X.; Yang, G.; Bai, W.; Sun, Y.; Du, Q.; Wang, X.; Qiu, T.; et al. Spaceborne GNSS Reflectometry with Galileo Signals on FY-3E/GNOS-II: Measurements, Calibration and Wind Speed Retrieval. *IEEE Geosci. Remote Sens. Lett.* **2023**, *20*, 1–5. [CrossRef]
31. Ulaby, F.T.; Long, D.G.; Blackwell, W.J.; Elachi, C.; Fung, A.K.; Ruf, C.; Sarabandi, K.; Zebker, H.A.; Van Zyl, J. *Microwave Radar and Radiometric Remote Sensing*; University of Michigan Press: Ann Arbor, MI, USA, 2014; Volume 4.
32. Kerr, Y.H.; Waldteufel, P.; Richaume, P.; Wigneron, J.P.; Ferrazzoli, P.; Mahmoodi, A.; Al Bitar, A.; Cabot, F.; Gruhier, C.; Juglea, S.E. The SMOS soil moisture retrieval algorithm. *IEEE Trans. Geosci. Remote Sens.* **2012**, *50*, 1384–1403. [CrossRef]
33. O'Neill, P.; Chan, S.; Njoku, E.; Jackson, T.; Bindlish, R. *SMAP Algorithm Theoretical Basis Document: L2 & L3 Soil Moisture (Passive) Products*; Jet Propulsion Laboratory: Pasadena, CA, USA, 2021.

34. Mironov, V.L.; Kosolapova, L.G.; Fomin, S.V. Physically and mineralogically based spectroscopic dielectric model for moist soils. *IEEE Trans. Geosci. Remote Sens.* **2009**, *47*, 2059–2070. [CrossRef]
35. Hengl, T. Clay Content in % (kg/kg) at 6 Standard Depths (0, 10, 30, 60, 100 and 200 cm) at 250 m Resolution (v0.2) [Data Set]. *Zenodo*. Available online: https://zenodo.org/record/2525663#.Y-7VR2lByUk (accessed on 10 October 2022).